**(Published by Nanomaterials, https://doi.org/10.3390/nano13020250)**

# Diethanolamine Modified Perovskite-Substrate Interface forRealizing Efficient ESL-Free PSCs

Sajid Sajid [1,2], Salem Alzahmi [1,2,*], Dong Wei [3], Imen Ben Salem [4], Jongee Park [5] and Ihab M. Obaidat [2,6,*]

[1] Department of Chemical & Petroleum Engineering, United Arab Emirates University, Al Ain P.O. Box 15551, United Arab Emirates

[2] National Water and Energy Center, United Arab Emirates University, Al Ain P.O. Box 15551, United Arab Emirates

[3] College of Physics and Energy, Fujian Normal University, Fuzhou 350007, China

[4] College of Natural and Health Sciences, Zayed University, Abu Dhabi P.O. Box 144534, United Arab Emirates

[5] Department of Metallurgical and Materials Engineering, Atilim University, Ankara 06836, Turkey

[6] Department of Physics, United Arab Emirates University, Al Ain P.O. Box 15551, United Arab Emirates

*****Correspondence: s.alzahmi@uaeu.ac.ae (S.A.); iobaidat@uaeu.ac.ae (I.M.O.)

**Abstract:** Simplifying device layout, particularly avoiding the complex fabrication steps and multiple high-temperature treatment requirements for electron-selective layers (ESLs) have made ESL-free perovskite solar cells (PSCs) attractive. However, the poor perovskite/substrate interface and inadequate quality of solution-processed perovskite thin films induce inefficient interfacial-charge extraction, limiting the power conversion efficiency (PCEs) of ESL-free PSCs. A highly compact and homogenous perovskite thin film with large grains was formed here by inserting an interfacial monolayer of diethanolamine (DEA) molecules between the perovskite and ITO substrate. In addition, the DEA created a favorable dipole layer at the interface of perovskite and ITO substrate by molecular adsorption, which suppressed charge recombination. Comparatively,

PSCs based on DEA-treated ITO substrates delivered PCEs of up to 20.77%, one of the highest among ESL-free PSCs. Additionally, this technique successfully elongates the lifespan of ESL-free PSCs as 80% of the initial PCE was maintained after 550 h under AM 1.5 G irradiation at ambient temperature.

**Keywords:** ESL-free perovskite solar cell; diethanolamine; interface modification; high performance

## 1. Introduction

Within the last few years, PSCs have progressed significantly in their PCEs, rising from 3.8 to 25.7% [1]. PSCs are conventionally fabricated using two architectures: planar and mesoscopic [2–6]. Mesoscopic PSCs are generally made up of an electron-selective layer (ESL), a mesoscopic $TiO_2$ or $Al_2O_3$ scaffold, a perovskite layer, a hole-selective layer (HSL), and back and front electrodes [7]. Further research found that PSCs can produce a PCE of over 15% utilizing a straightforward planar architecture, achieving high efficiency without the need for a mesoscopic scaffold [8–17]. Due to perovskite's ambipolar characteristic, additional device architectural simplification is possible in order to fabricate efficient PSCs without using complicated fabrication methods [18,19]. In this scenario, HSL-free PSCs can be produced without manufacturing or utilizing costly organic HSLs [20,21]. The subsequent focus in PSCs is on the simplified fabrication technique that offers simple and inexpensive mass production in order to become economically relevant in the context of high efficiency and reasonable stabilities [22]. In this context, numerous researchers constructed ESL-free PSCs with reasonable PCEs [23]. ESL-free PSCs have a high device stability potential in addition to decent PCEs and do not need the time- consuming manufacturing of ESLs, particularly the numerous high-temperature processes required to create $TiO_2$ ESL. Since it is known that $TiO_2$ causes the perovskite layer to decompose by creating oxygen vacancies, the removal of the $TiO_2$ ESL is mostly responsible for the high device stability [24]. However, because of the inefficient electron transport and the associated carrier recombination at the interface of transparent conductive oxides (TCO) and perovskite, the performance of ESL-free PSCs is still inferior to that of conventional devices [25–27]. An additional reason for the low device efficiency of the ESL-free PSCs is the rough and uneven perovskite film when no ESL is fabricated, which will produce many open grain boundaries and lead to severe recombination as a result of the shunt pathways between the HSL and TCO. Surface modification methods were recently suggested to reduce charge-carrier recombination at the TCO/perovskite interface and to initiate charge collection at the relevant contact [28,29].

The efficacy of the resulting ESL-free PSCs is enhanced by carefully adjusting the compositions, architecture, and morphology of the perovskite layer as well as pre-treating the TCO ($UV/O_3$ irradiation) to prevent carrier recombination in the perovskite or at the TCO/perovskite interface [24]. These ESL-free PSCs, however, displayed relatively lower PCEs (<18%) than those of their ESL-containing counterparts. Other methods for improving device performance and surface modification of TCO substrates include bathocuproine [25], polar non-conjugated small molecule modifier [30], and hydroxyethyl-functionalized imi- dazolium iodide ionic liquid [31], and self-assembled fullerene monolayer [32]. Recently, PCEs of ESL-free PSCs >19% have been reported employing sodium fluoride [33] and tetramethylammonium hydroxide [34] as TCO modifiers. Nevertheless, most of the modi- fications in the aforementioned approaches need additional or difficult processes, which consumes time and energy. These modifiers are also regarded for their hygroscopicity, insulating properties, and high material costs.

In the present study, we used a low-cost, very simple Indium-Tin Oxide (ITO)-surface modification with DEA to enhance the ITO/perovskite interaction and perovskite crys- tallization. Because amine groups typically interact with the ITO surface and Pb-based substances are reported to link with –OH groups, we chose DEA, which contains both –OH and amine groups, as the contact modifier between ITO and perovskite [35]. As anticipated, the DEA molecular interlayer interacted with ITO and perovskite, which strengthened the interface contact and elevated the crystallinity of the perovskite. A dipole layer that is well-orientated for electron extraction was also produced by molecular adsorption. The electron extraction rate was significantly improved as a result, and the ESL-free PSC with the ITO/DEA/Perovskite/spiro/Au device structure demonstrated significantly better performance (PCE: 20.77%) than an ITO/Perovskite/spiro/Au device (PCE: 18.65%).

## 2. Experimental Procedure

### *2.1.Solution Preparation*

Perovskite solution was obtained by mixing anhydrous dimethylformamide/dimeth- ylsulfoxide (600 mg/78 mg) with 0.15 M of formamidinium lead iodide (FAI), 0.85 M of methylammonium lead iodide (MAI), and 1.025 M of $PbI_2$. This solution was stirred for 4 h in a glove box. Spiro-OMeTAD was dissolved in chlorobenzene at a concentration of 80 mg/mL to make the precursor for the hole-selective layer. Tert-butylpyridine (28.5 µL in 1 mL of chlorobenzene) and lithium bis-(trifluoromethanesulfonyl) imide (8.75 mg/mL) were then added as additives, and the mixture was stirred in a glove box for 6 h.

### *2.2.Device Fabrication*

The ITO substrates were ultrasonically cleaned with detergent solution, deionized water, acetone, ethyl alcohol, and deionized water for 20 min, respectively. The ITO substrates were exposed to UV-ozone for 20 min after drying. The cleaned ITO substrates were spin-coated with the DEA pure solvent for 30 s at 2000 rpm and then dried for 10 min at 100 °C. The bare cleaned ITO and DEA-treated ITO substrates were spin-coated with the perovskite precursor at 4000 rpm for 25 s to form the perovskite layers. Eighteen seconds before the end of the spin-coating process, 0.8 mL of diethyl ether was dripped on the perovskite surface. The resulting perovskite layers were heated for 15 min at 130 °C before naturally cooling to ambient temperature. Subsequently, both perovskite layers were spin-coated with the Spiro-OMeTAD solution for 30 s at 4000 rpm. The devices were finished by evaporating 60 nm Au electrodes onto the ITO/perovskite/spiro-OMeTAD and ITO/DEA/perovskite/spiro-OMeTAD.

*2.3. Characterizations*

A Thermo Fisher Scientific (Shanghai, China) ESCALAB 250Xi under $10^{-9}$ Torr vac- uum with a monochromatic Al-$K_\alpha$ X-ray source was used to collect the XPS spectra. A scanning electron microscope (Hitachi, Chiyoda, Japan, S-4800) and an atomic force microscope (Agilent Keysight (Beijing, China) AFM-5500) were utilized to study the mor- phologies. The perovskite's crystallinity was examined using an X-ray diffractometer (Bruker D8 Advance (Bruker AXS Inc.), Cu-$K_\alpha$ radiation of 0.15406 nm). The UPS spectra were obtained using the ESCALAB 250Xi Contact angle images were obtained with an Ossila Contact Angle Goniometer. The FT-IR spectra were collected by using a Jasco (Tokyo, Japan) FT-IR spectrometer. Using a UV-Vis spectrophotometer (UV-2600), the absorption spectrum was measured. The steady-state PL spectra of the produced samples were looked at utilizing an Edinburgh PLS 980. Utilizing a transient state spectrophotometer (Edin- burgh Institute F900) and a 485 nm laser, the TRPL decay of the perovskite layers was monitored. Under AM 1.5 G illumination with a power intensity of 100 mW $cm^{-2}$, the *J-V* characteristic curves were measured with a source meter (Keithley (Cleveland, OH, USA) 2400) utilizing forward ( 0.1 to 1.2 V) or reverse (1.2 to 0.1 V) scans from a solar simulator (XES-301S+EL-100). The delay time was set to 10 ms, and the step voltage was set to 12 mV. The EQE was calculated using QE-R systems (Enli Tech., Shanghai, China). The EIS measurement was carried out using an electrochemical workstation (Zahner Zennium). The EIS data were fitted with help of ZSim-software version 3.20 with equivalent circuit parameters of $R_1$ = 0.116, C = 0.00001 and $R_2$ = 54.1 (for ITO-based device), and $R_1$ = 0.116, C = 0.000001 and $R_2$ = 29.6 (for DEA-treated ITO-based device).

## 3. Results and Discussion

The cleaned ITO substrates were first spin-coated with DEA at 2000 rpm for 30 s, then dried at 100 °C for 10 min. X-ray photoelectron spectroscopy (XPS) was carried out to investigate the effect of DEA treatment on the surface chemistry of ITO. The XPS survey spectra of bare ITO and DEA-treated ITO are presented in Figure 1. All spectra were calibrated using the C 1s peak of 284.9 eV binding energy as a reference point. The bare ITO and DEA-treated ITO share the same peaks except at 400.4 eV, which is assigned to N 1s, showing that the DEA successfully adsorbed on the ITO substrate, as can be seen in Figure 1a,b. Figure 1c displays the high-resolution N 1s spectra of ITO/DEA, which can be divided into three peaks at 401.4, 400.4, and 399.7 eV. Sigma-state, including species containing N, can be attributed to the peaks at 401.4 eV and 400.4 eV. Additionally, it has been stated that an amine group correlates to the peak at 399.7 eV [36,37]. The shift in the binding energy, as observed in the Sn 3d (Figure 1d) signals, is indicative of a chemical interaction between DEA and the ITO substrate. This suggests a dipole interaction between ITO and DEA that is mediated by an electric field, which lowers the attractive force of the Sn nuclei and increases the Sn atom's outer-shell electron density [38].

To investigate the impact of DEA coating on the surface morphology of ITO, scanning electron microscopy (SEM) was conducted on bare ITO and DEA-treated ITO. Figure 2a,b displays the surface SEM images of ITO and ITO/DEA, respectively. As can be seen, both surfaces are compact without pinholes. However, because the DEA layer is so thin, it is hard to see the DEA-coated ITO surface clearly. Figure S1 shows that this thin layer of DEA had little influence on ITO transparency across a wide spectrum of light, indicating a great potential for high photocurrent output. The morphologies of the bare ITO and DEA-treated ITO were investigated with the help of atomic force microscopy (AFM), as shown in Figure 2c,d. The alteration in the morphology following DEA coating is not very noticeable, similar to the SEM images. However, in the DEA-treated ITO substrate, a reasonable decrease in the root-mean-square (RMS) of surface roughness from 2.8 to 0.9 nm is observed. The DEA coating may considerably minimize the surface defect states and promote the deposition of high-quality perovskite thin film because of the reduced roughness. We also used Kelvin probe force microscopy (KPFM) to examine bare and DEA- treated ITO, as displayed in Figure S2. This revealed that the surface potential distribution is consistent with the aforementioned surface morphologies, and the average potential of the ITO/DEA substrate is 110 mV compared to the 0.18 mV of bare ITO, which indicates desirable Fermi-level of the ITO/DEA and better band alignment with perovskite [24,39].

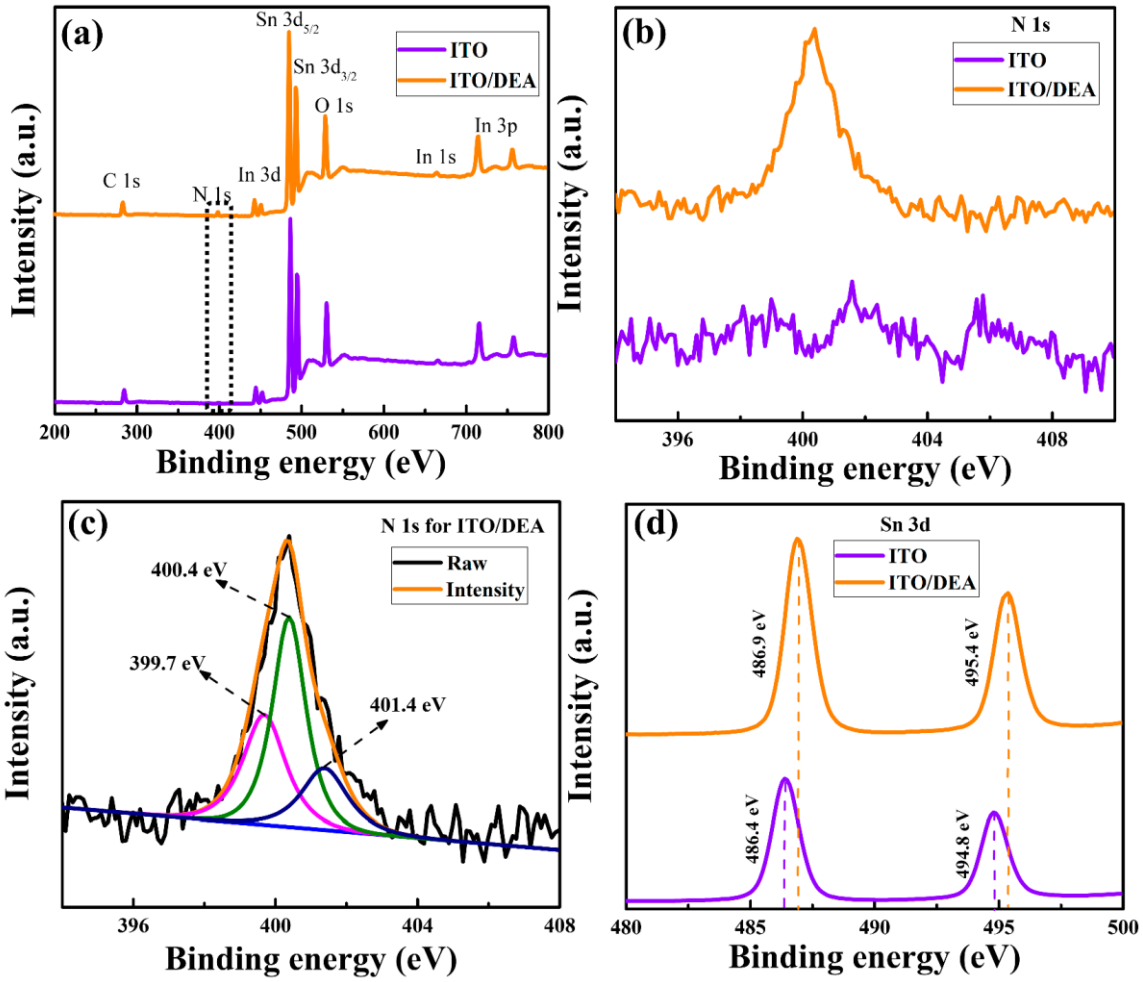


**Figure 1.** XPS spectra of ITO substrate and ITO/DEA substrate (**a**), N 1s spectra of ITO substrate and ITO/DEA substrate (**b**), analysis of N 1s spectra of ITO/DEA substrate (**c**), and Sn 3d spectra of ITO substrate and ITO/DEA substrate (**d**).

In order to get highly efficient PSCs in ESL-free architectures, one of the main obstacles is the energy-level mismatch between ITO and the perovskite, so it is essential to investigate how DEA affects the energy levels of ITO. Figure 3a,b illustrates the outcomes of an ultraviolet photoelectron spectroscopy (UPS) experiment. For the purpose of calculating $E_{cutoff}$ (secondary electron edges) and $E_{onset}$ (Fermi edges), the intercepts of the tangents of the peaks with the extrapolated baselines were used. By estimating the difference between the incident photon energy (light source He I, 21.22 eV) and $E_{cutoff}$, the Fermi-level ($E_F$) values of the bare and DEA-treated ITO were quantitatively determined. The UPS show an $E_{cutoff}$ of 16.64 eV and 17.21 eV for bare ITO and ITO/DEA, respectively. The $E_F$ values of bare ITO and ITO/DEA were estimated to be 4.58 and 4.01 eV, respectively, using the following equation.

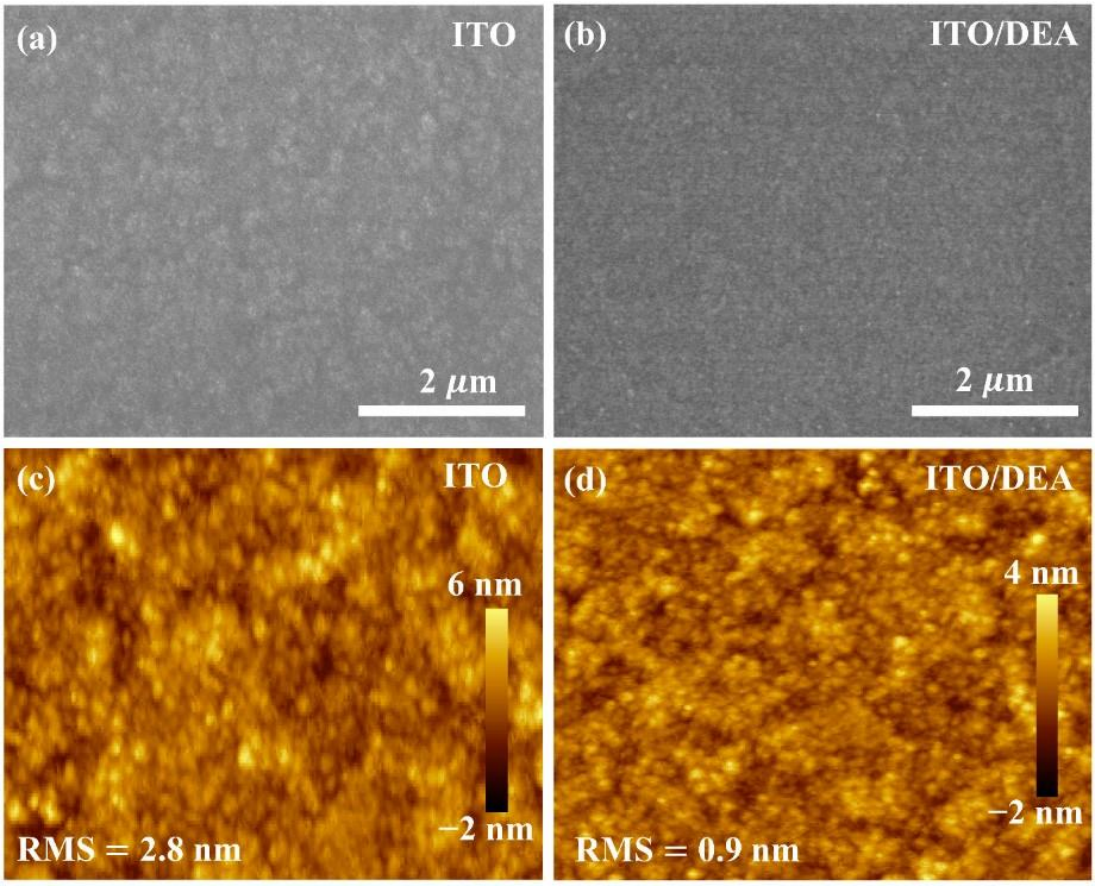


**Figure 2.** SEM images of the ITO substrate (**a**), ITO/DEA substrate (**b**), AFM images of ITO substrate (**c**), and ITO/DEA substrate (**d**).

The $E_F$ of the ITO was significantly shifted by 0.57 eV after DEA treatment, which would be advantageous for the cathode's ability to collect electrons. This is because, following DEA treatment, a favorable dipole moment formed on the surface of the ITO. As stated in previous studies, Pb-based compounds interact with –OH groups, while the amine groups in DEA tend to link with the ITO surface [34,35]. As can be seen, the DEA modification resulted in a 0.57 eV shift in the Fermi level of ITO, which should be attributed to a chemical reaction between DEA and ITO, as supported by the FT-IR data (Figure S4). The appearance of the N-atom signal in Figure 1 demonstrates the interaction between the N-atom of DEA and ITO. The -NH- (from the amine group) should function as an electron donor to engage in chemisorption and modify the energy levels of ITO. To examine the surface wettability of ITO treated with DEA, the water contact angle was measured (Figure 3c). Since DEA possesses hydrophilic –OH and amine groups, the water contact angles of the ITO surface decrease from 70.1° to 59.6°, showing greater wetting capabilities of DEA-treated ITO. The superior wettability can decrease the nucleation barrier and aid in the formation of a high-quality perovskite layer.

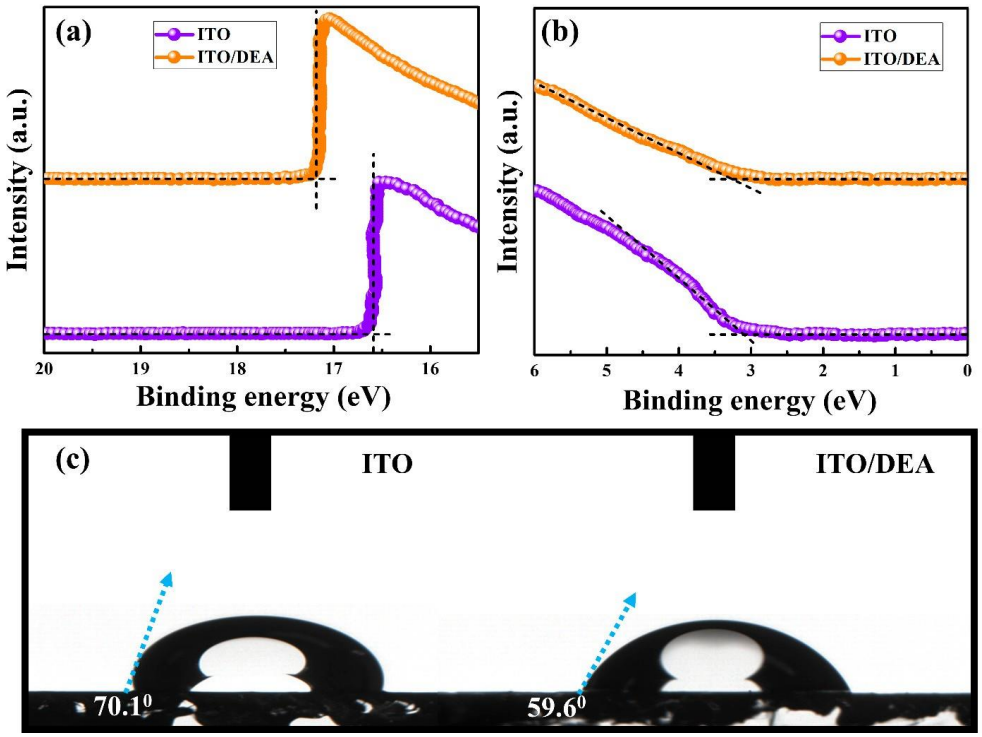


**Figure 3.** UPS spectra of ITO substrate and ITO/DEA substrate (**a**,**b**), and the contact angle pho-tographs of water droplets on ITO substrate and ITO/DEA substrate (**c**).

The surface morphologies and cross-sectional images of the perovskite layers prepared on bare ITO and ITO/DEA substrates were taken with help of SEM, as depicted in Figure 4. It is evident that the perovskite layers that were formed on ITO/DEA have densely packed, considerably larger grains. In order to facilitate charge transfer, the perovskite layer formed on ITO/DEA substrate displays entire coverage without any grain boundary gaps. The larger perovskite grains and improved morphology on the ITO/DEA substrate can be attributed to the favorable interaction of the –OH group with $Pb^{2+}$ [35], which promotes the formation of larger grains and passivation of the perovskite's grain boundaries. A schematic representation of the DEA interaction is shown in Figure S3a, where the –OH groups of the DEA would interact with the Pb-atoms in the perovskite thin film while the N-atom of DEA tends to create a chemical connection with the Sn atom on the ITO surface. According to other researchers, the interaction between the –OH group and $Pb^{2+}$ can improve the penetration of $PbI_2$ into a $TiO_2$ mesoporous layer [40]. Through the direct mixing of DEA solution and $PbI_2$ powder, we were able to further test the possible interaction between DEA and $PbI_2$. Intriguingly, adding $PbI_2$ to DEA has significantly altered the appearance, likely creating new products. As seen in Figure S3b, the colorless DEA solution and the yellow $PbI_2$ powder were combined to create an entirely distinct product that was white in color. The white mixture turns into a colorless liquid after heating (Figure S3c). To further confirm these interactions, Fourier-transform infrared (FT-IR) spectra in the

wavenumber range of 600 to 4000 $cm^{-1}$ were carried out, as shown in Figure S4. The spectrum of the ITO substrate shows typical broad bands below 800 $cm^{-1}$, which is assigned to the stretching vibration of In-O or Sn-O bonds [41]. The DEA-modified ITO shows broad and strong bands below 800 $cm^{-1}$. In addition to the broad and strong bands, the DEA-modified ITO displays an additional sharp and strong peak at 630 $cm^{-1}$, which is ascribable to the stretching vibration of the Sn-N bond. Therefore, it is reasonable to assume that the DEA and ITO substrate were linked by a Sn-N bond, exposing the –OH groups for interaction with the perovskite layer that was later added. The DEA and $PbI_2$/DEA were characterized using FT-IR spectroscopy, and the variation in –OH absorption peak was monitored. Broad absorption peaks can be seen in the DEA and DEA/$PbI_2$ spectra between 1052 and 1458 $cm^{-1}$, which corresponds to the scissoring vibration of the –OH group, as seen in Figure S4b. The peak locations altered in the $PbI_2$/DEA sample from 1052–1458 $cm^{-1}$ to 1044–1448 $cm^{-1}$, indicating a connection between $PbI_2$ and the –OH groups of DEA. As seen in Figure S3b, the addition of $PbI_2$ to DEA has significantly altered the appearance, perhaps creating new compounds. These observations point to a significant interaction between DEA and $PbI_2$. In perovskite deposition, the exposed –OH groups on the ITO surface would interact favorably with the $PbI_2$, which is present in the perovskite precursor solution. An even and complete coverage of the perovskite layer would benefit from this advantageous interaction, ensuring good interface contact with the ITO/DEA substrate.

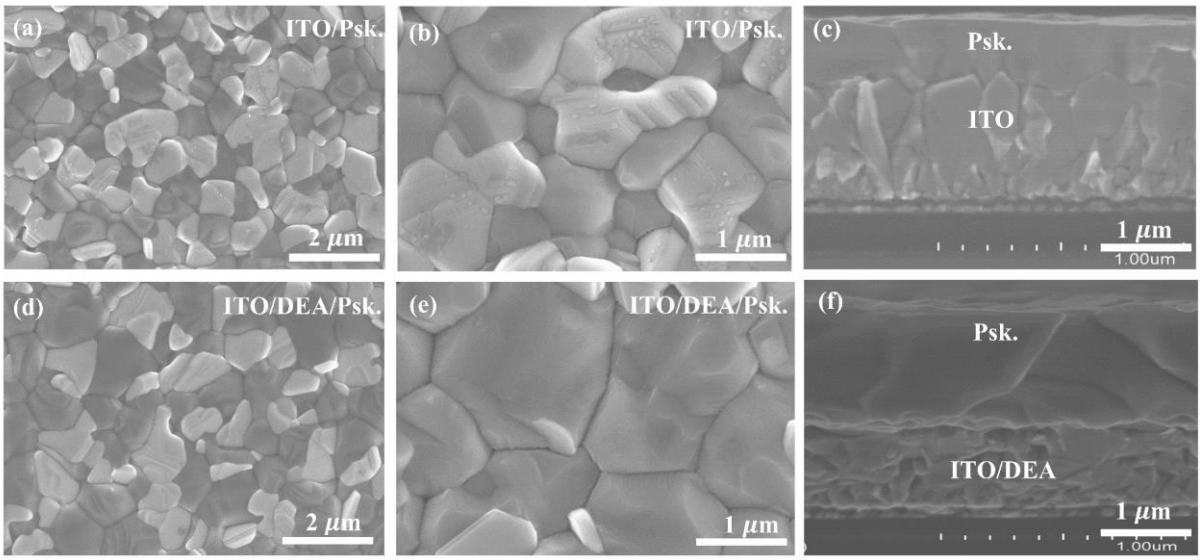


**Figure 4.** SEM images of the surface and cross-section of the perovskite (Psk.) layers prepared on ITO substrates (**a**–**c**) and ITO/DEA substrates (**d**–**f**), respectively.

The formation of high-quality perovskite layers may improve the performance of corresponding PSCs by facilitating charge transport and reducing recombination losses [42]. In addition to morphological characteristics, X-ray diffraction (XRD) and UV-vis absorp-tion spectra were used to study how DEA deposition affected the structure and optical performance of the perovskite layers. The high-intensity peaks from the XRD pattern of the perovskite layer formed on ITO/DEA displayed slightly greater crystallinity com- pared to bare ITO, as shown in Figure 5a. Additionally, the perovskite layer formed on the ITO/DEA substrate exhibits slightly greater absorption capabilities throughout the entire spectral region as evidenced by UV-vis absorbance spectra in Figure 5b. Steady-state photoluminescence (PL) and time-resolved PL (TRPL) measurements were used to analyze the charge-carrier dynamics of perovskite layers grown on glass, bare ITO, and ITO/DEA substrates, as shown in Figure 5c,d. When compared to perovskite layers formed on glass and glass/ITO, the PL spectra in Figure 5c show a considerable drop in intensity for the ITO/DEA substrate, suggesting higher electron transfer to the corresponding layer [43] and lower recombination of charges [44]. A significant quenching effect for the perovskite layer deposited on the ITO/DEA substrate can be seen in the TRPL spectra given in Figure 5d, demonstrating the improved electron extraction capability from the perovskite layer to the DEA-treated substrate. The results were fitted by a biexponential decay function with the following equation where $\tau_1$ and $\tau_2$ represent decay factors that are closely related to non-radiative recombination by defects and a component of bulk recombination, respectively. Table S1 shows decreased values for $\tau_1$ and $\tau_2$ for the perovskite layer deposited. on the ITO/DEA substrate, indicating minimized recombination losses.

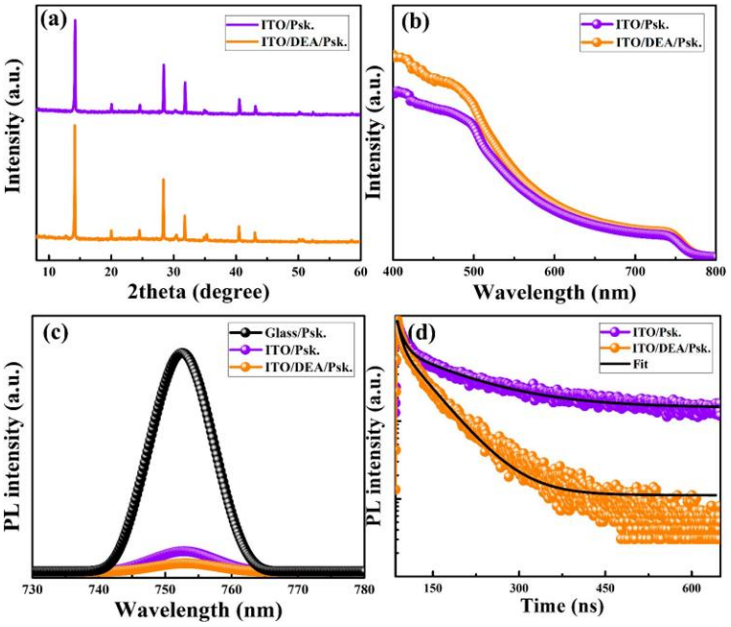


**Figure 5.** XRD patterns (**a**), UV-Vis spectra (**b**), PL-spectra (**c**), and TRPL-spectra (**d**) of the ITO/perovskite and ITO/DEA/perovskite, respectively.

We fabricated PSCs with and without DEA for the evaluation of photovoltaic param-eters after carefully examining the morphology and substantial role of the DEA at the ITO/perovskite interface. The schematic diagram of the as-prepared device and energy levels of each layer are depicted in Figure S5. The cross-sectional SEM images, current- voltage (*J-V*) characteristic curves, and photovoltaic parameters of the as-prepared PSCsare depicted in Figure 6 and Table 1, respectively. The PSC employing bare ITO displays an open-circuit voltage ($V_{oc}$) of 1.096 V, a short-circuit current density ($J_{sc}$) of 22.94 mA $cm^{-2}$, a fill factor (FF) of 74.19%, and a power conversion efficiency (PCE) of 18.65% under reverse scan condition. In comparison, the DEA-modified PSC shows improved performance of upto PCE of 20.77%, a $V_{oc}$ of 1.109 V, a $J_{sc}$ of 24.45 mA $cm^{-2}$, and an FF of 76.60% under the same scan condition. It is noteworthy that the DEA-modified PSC exhibits significantly better performance and less hysteresis in the *J-V* curves. The better layer quality and im-proved charge-carrier transport at the ITO/DEA/perovskite interface might be primarilyresponsible for the improved performance and decreased hysteresis, which is consistent with the dark *J-V* curves, as discussed below, where we observed a decrease in the density of trap states in the DEA-modified PSCs.

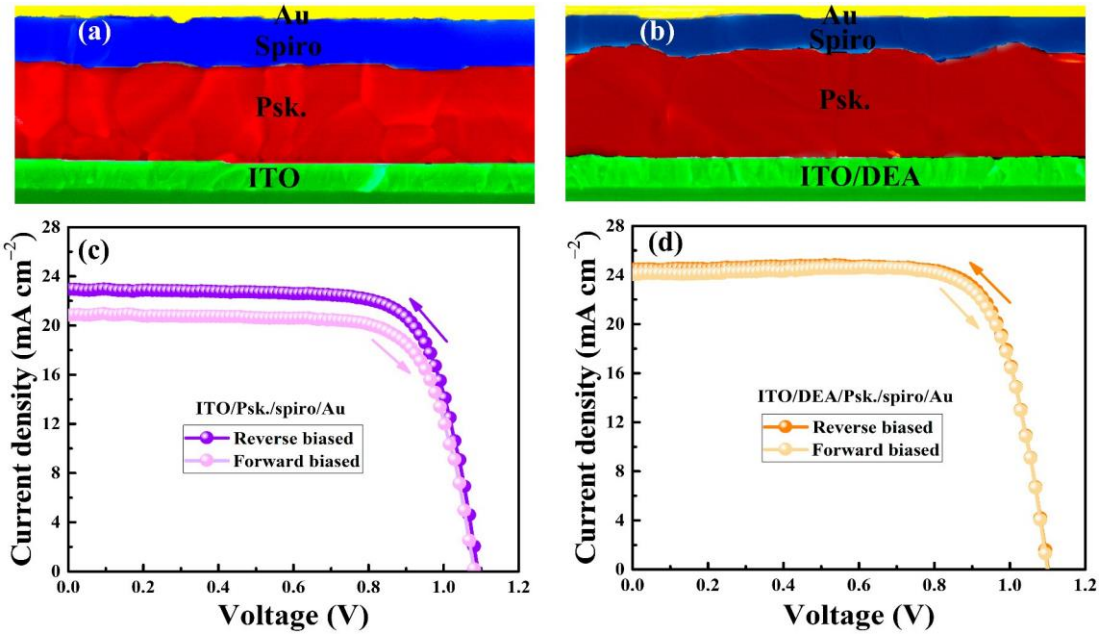


**Figure 6.** Cross-sectional SEM images of as-fabricated devices with ITO substrate (**a**) and ITO/DEA substrate (**b**). The *J-V* characteristic curves of devices fabricated with ITO substrate (**c**) and ITO/DEA substrate (**d**).

**Table 1.** Photovoltaic parameters of the PSCs under forward bias and reverse bias.

| | | | | | (%) |
|---|---|---|---|---|---|
| ITO/Psk./spiro/Au | Reverse | 1.096 | 22.94 | 74.19 | 18.65 |
| | Forward | 1.083 | 20.83 | 74.24 | 16.75 |
| ITO/DEA/Psk./spiro/Au | Reverse | 1.109 | 24.45 | 76.60 | 20.77 |
| | Forward | 1.096 | 24.02 | 77.94 | 20.52 |

To further confirm the charge-carrier dynamics and charge-carrier recombination in the devices with bare ITO and ITO/DEA, the dark *J-V* measurement was carried out. As seen in Figure 7a, the device with DEA has a lower current density than the device with bare ITO. This shows that the DEA/perovskite interface has efficient charge transport. In order to quantitatively assess the trap density in the as-prepared devices, we also fabricated electron-only devices (ITO/Perovskite/PCBM/Au and ITO/DEA/perovskite/PCBM/Au), as shown in Figure 7b. The trap density ($N_{trap}$) can be determined with the equation where $\varepsilon_0$, $\varepsilon$, $V_{TFL}$, $e$, and $L$ are the vacuum permittivity, relative dielectric constant, trap- field limit voltage, elementary charge, and perovskite layer thickness, respectively. Since $N_{trap}$ and $V_{TFL}$ are linearly related, a device with a smaller $V_{TFL}$ will exhibit fewer defects overall. As seen in Figure 7b, the device with DEA exhibits a significantly lower $V_{TFL}$ (0.25 V) than the device with bare ITO (0.33 V), indicating DEA successfully reduces the defect density. The smooth morphology with fewer grain boundaries and the high-quality crystallinity of the perovskite layer deposited on the ITO/DEA substrate are responsible for the reduced trap density. Electrochemical impedance spectroscopy (EIS) measurements were conducted in order to learn more about how DEA affects the interfacial charge transport and recombination processes in the PSCs. Figure 7c displays the Nyquist plots of the corresponding devices with a bias voltage of 0.9 V under dark conditions and a frequency range of 1 Hz to 1 MHz. At higher frequencies, the semicircle stands in for the charge transport resistance ($R_{ct}$), which originates from the substrate and perovskite contact. Because ITO/DEA made better contact with the perovskite surface, the DEA-treated PSC showed a lower $R_{ct}$ value (29.76 kΩ) than the ITO-based device ($R_{ct}$ of 54.06 kΩ), indicating more efficient electron transfer and electron extraction at the corresponding interface. Additionally, measurements of external quantum efficiency (EQE) were made in order to assess how well the *J-V* and EQE curves agreed. The matching $J_{sc}$ values integrated from the EQE curves (Figure 7d) for both devices are consistent with *J-V* characteristic curves. Here, we noticed a minor discrepancy between the EQEs of the PSCs and the absorption spectra of the perovskite layers prepared on ITO and DEA-treated ITO substrates in the range of 400–500 nm. This can be attributed to the

fact that the absorption spectra do not represent an external property of the PSCs but rather an internal property of the perovskites (originating from the distinctive energy-band structure) [45–47]. Moreover, the EQE spectrum encompasses all excitonic and/or thermal broadening effects, along with the architectural features of the PSC, and this reflects the occupied density of states as specified in the entire PSC rather than in individual perovskites.

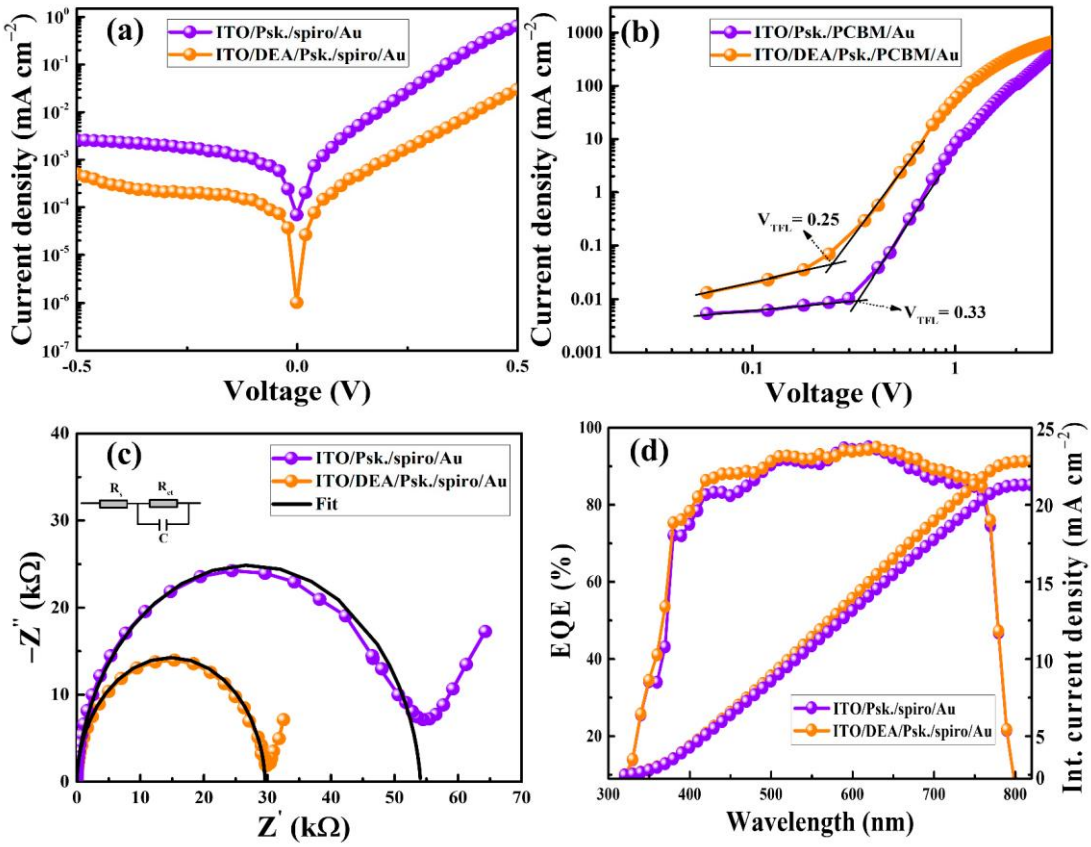


**Figure 7.** Dark *J-V* curves of as-prepared devices (**a**) and electron-only devices (**b**), EIS measurement (**c**), and EQEs with integrated $J_{SC}$ of the PSCs prepared using ITO substrates and ITO/DEA substrates (**d**).

Furthermore, we acquired performance data from 9 PSCs with bare ITO and ITO/DEA, respectively, to show the reproducibility of the devices. The ITO/DEA-based PSCs exhibit improved performance and reproducibility when compared to PSCs with bare ITO, as shown in Figure S6. In addition to the high PCEs, the PSCs should have long-term stability. Figure 8a illustrates the tracking of the steady-state PCEs of the PSCs with ITO/DEA and bare ITO under AM 1.5 G at maximum power at 0.9 V bias voltage and ambient temperature. After 120 s of continuous illumination, the ITO/DEA-based device showed a stabilized PCE of 19.71%, which is considerably near the

highest PCE of 20.77% for the same PSC. Additionally, for 550 h of AM 1.5 G irradiation, the stabilities of the unsealed PSCs made with bare ITO and ITO/DEA substrates were evaluated every 34 h. After each stability test, the tested PSCs were kept in a glass oven at 60% humidity and 25 ˚C. Figure 8b demonstrates how the stability of the ITO/DEA-based PSCs exceeded that of the ITO-based devices. After 550 h, the ITO/DEA-based PSC still had 80% of the original PCE. The bare ITO-based PSCs under the same testing conditions only retained 37% of the initial PCE, demonstrating poor stability and quick degradation. The degradation of ITO-based PSCs is associated with rapid erosion because the perovskite layer formed on the bare ITO substrate has a defective surface morphology. As mentioned above, high-quality perovskite layers were created on the DEA-treated ITO substrates, with compact, large grains, and reduced grain boundaries. Starting from the grain boundaries makes it considerably easier to decompose perovskite films. Less oxygen, water, etc. will intermix within the grain boundaries of the perovskite films because there are fewer grain boundaries. The stability of PSCs made using DEA-treated ITO substrates is ultimately improved by the perovskite film with fewer grain boundaries, which effectively shields perovskite films from water penetration. Conversely, erosion occurs more rapidly in the perovskite thin films generated using the ITO substrates because these have a considerably rougher surface with smaller grain sizes and numerous grain boundaries.

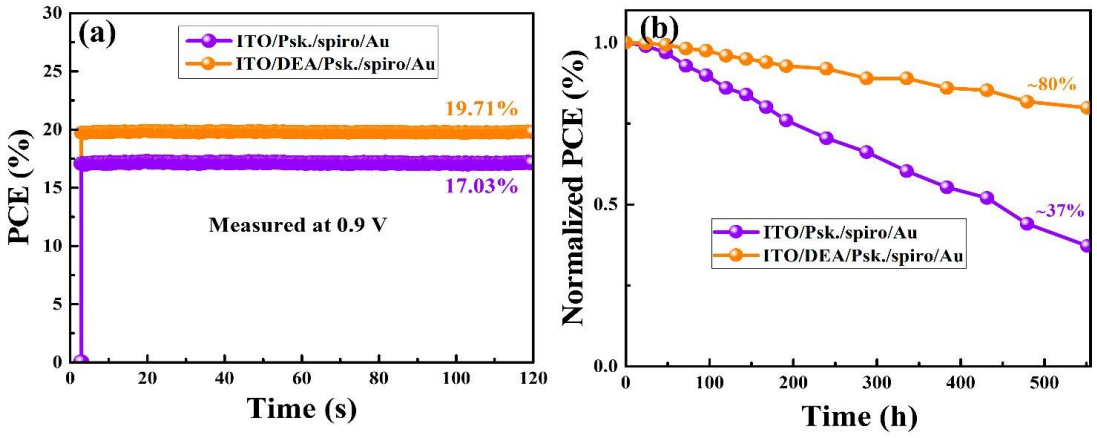


**Figure 8.** Stability analyses of the PSCs prepared with ITO substrates and ITO/DEA substrates. PCE at maximum power point tracking under continuous illumination of AM 1.5 G irradiation (**a**) and Normalized PCE for 550 h under AM 1.5 G irradiation (**b**).

## 4. Conclusions

We used DEA to generate Sn-N and –OH–Pb chemical linkages between the perovskite layer and the ITO substrate. The interface contact, perovskite crystallinity, and film quality have all increased due to these chemical interactions, and the perovskite layer's grain boundaries and trap states have decreased. Based on the creation of interfacial dipole layers, our results imply that the addition of DEA can modify the band misfit at the ITO/perovskite contact, hence reducing the voltage deficits. Transient PL, TRPL, and IS measurements revealed that the rates of electron extraction and charge transfer have dramatically improved. The PCE of the PSCs has significantly increased as a result, rising from about 18.65% to 20.77%. Additionally, DEA modification has increased the stability of the PSCs, with 80% PCE retention even after 550 h without encapsulation. This is likely because the DEA modification improved the interfacial contact and thin-film quality of the perovskite. Our research opens up scientific pathways for the facile fabrication of ESL-free PSCs.

**References**


1. Green, M.; Dunlop, E.; Hohl-Ebinger, J.; Yoshita, M.; Kopidakis, N.; Bothe, K.; Hinken, D.; Rauer, M.; Hao, X. Solar cell efficiency tables (Version 60). *Prog. Photovolt. Res. Appl.* **2022**, *30*, 687–701.
2. Sajid, S.; Elseman, A.; Huang, H.; Ji, J.; Dou, S.; Jiang, H.; Liu, X.; Wei, D.; Cui, P.; Li, M. Breakthroughs in $NiO_X$-HTMs towards stable, low-cost and efficient perovskite solar cells. *Nano Energy* **2018**, *51*, 408–424.
3. Sajid, S.; Elseman, A.; Ji, J.; Dou, S.; Wei, D.; Huang, H.; Cui, P.; Xi, W.; Chu, L.; Li, Y.; et al. Computational Study of Ternary Devices: Stable, Low-Cost, and Efficient Planar Perovskite Solar Cells. *Nano-Micro Lett.* **2018**, *10*, 51.
4. Sajid, S.; Khan, S.; Khan, A.; Khan, D.; Issakhov, A.; Park, J. Antisolvent-fumigated grain growth of active layer for efficient perovskite solar cells. *Sol. Energy* **2021**, *225*, 1001–1008.
5. Sajid, S.; Elseman, A.; Wei, D.; Ji, J.; Dou, S.; Huang, H.; Cui, P.; Li, M. NiO@carbon spheres: A promising composite electrode for scalable fabrication of planar perovskite solar cells at low cost. *Nano Energy* **2019**, *55*, 470–476.
6. Sajid, S.; Alzahmi, S.; Salem, I.; Obaidat, I. Guidelines for Fabricating Highly Efficient Perovskite Solar Cells with $Cu_2O$ as the Hole Transport Material. *Nanomaterials* **2022**, *12*, 3315.
7. Im, J.-H.; Lee, C.-R.; Lee, J.-W.; Park, S.-W.; Park, N.-G. 6.5% efficient perovskite quantum-dot-sensitized solar cell. *Nanoscale* **2011**,*3*, 4088–4093.
8. Elseman, A.; Shalan, A.; Sajid, S.; Rashad, M.; Hassan, A.; Li, M. Copper-Substituted Lead Perovskite Materials Constructed with Different Halides for Working $(CH_3NH_3)2CuX_4$-Based Perovskite Solar Cells from Experimental and Theoretical View. *ACS Appl. Mater. Interfaces* **2018**, *10*, 14.
9. Sajid, S.; Elseman, A.; Ji, J.; Dou, S.; Huang, H.; Cui, P.; Wei, D.; Li, M. Novel hole transport layer of nickel oxide composite with carbon for high-performance perovskite solar cells. *Chin. Phys. B* **2018**, *27*, 17305.
10. Wei, D.; Ma, F.; Wang, R.; Dou, S.; Cui, P.; Huang, H.; Ji, J.; Jia, E.; Jia, X.; Sajid, S.; et al. Ion-Migration Inhibition by the Cation–π Interaction in Perovskite Materials for Efficient and Stable Perovskite Solar Cells. *Adv. Mater.* **2018**, *30*, 1707583.
11. Elseman, A.; Sharmoukh, W.; Sajid, S.; Cui, P.; Ji, J.; Dou, S.; Wei, D.; Huang, H.; Xi, W.; Chu, L.; et al. Superior Stability and Efficiency over 20% Perovskite Solar Cells Achieved by a Novel Molecularly Engineered Rutin–AgNPs/Thiophene Copolymer. *Adv. Sci.* **2018**,

*5*, 1800568.

12. Sajid, S.; Huang, H.; Ji, J.; Jiang, H.; Duan, M.; Liu, X.; Liu, B.; Li, M. Quest for robust electron transporting materials towards efficient, hysteresis-free and stable perovskite solar cells. *Renew. Sustain. Energy Rev.* **2021**, *152*, 111689.
13. Khan, D.; Sajid, S.; Khan, S.; Park, J.; Ullah, I. Identifying the potentials for charge transport layers free n-p homojunction-based perovskite solar cells. *Sol. Energy* **2022**, *238*, 69–77.
14. Elseman, A.; Sajid, S.; Shalan, A.; Mohamed, S.; Rashad, M. Recent progress concerning inorganic holetransport layers for efficient perovskite solar cells. *Appl. Phys. A* **2019**, *125*, 476.
15. Wei, D.; Huang, H.; Cui, P.; Ji, J.; Dou, S.; Jia, E.; Sajid, S.; Cui, M.; Chu, L.; Li, Y.; et al. Moisture-tolerant supermolecule for the stability enhancement of organic–inorganic perovskite solar cells in ambient air. *Nanoscale* **2019**, *11*, 1228–1235.
16. Huang, H.; Yan, H.; Duan, M.; Ji, J.; Liu, X.; Jiang, H.; Liu, B.; Sajid, S.; Cui, P.; Li, Y.; et al. $TiO_2$ surface oxygen vacancy passivation towards mitigated interfacial lattice distortion and efficient perovskite solar cell. *Appl. Surf. Sci.* **2021**, *544*, 148583.
17. Huang, H.; Liu, X.; Duan, M.; Ji, J.; Jiang, H.; Liu, B.; Sajid, S.; Cui, P.; Wei, D.; Li, Y.; et al. Dual Function of Surface Alkali-Gas Erosion on $SnO_2$ for Efficient and Stable Perovskite Solar Cells. *ACS Appl. Energy Mater.* **2020**, *3*, 5039–5049.
18. Stranks, S.; Eperon, G.; Grancini, G.; Menelaou, C.; Alcocer, M.; Leijtens, T.; Herz, L.; Petrozza, A.; Snaith, H. Electron-hole diffusion lengths exceeding 1 micrometer in an organometal trihalide perovskite absorber. *Science* **2013**, *342*, 341–344.
19. Dong, Q.; Fang, Y.; Shao, Y.; Mulligan, P.; Qiu, J.; Cao, L.; Huang, J. Electron-hole diffusion lengths >175 μm in solution-grown $CH_3NH_3PbI_3$ single crystals. *Science* **2015**, *347*, 967–970.
20. Wu, W.-Q.; Wang, Q.; Fang, Y.; Shao, Y.; Tang, S.; Deng, Y.; Lu, H.; Liu, Y.; Li, T.; Yang, Z. Molecular doping enabled scalable blading of efficient hole-transport-layer-free perovskite solar cells. *Nat. Commun.* **2018**, *9*, 1–8.
21. Zhang, J.; Sun, Y.; Yu, H. Reducing energy loss via adjusting the anode work function and perovskite layer morphology for the efficient and stable hole transporting layer-free perovskite solar cells. *Chem. Eng. J.* **2022**, *431*, 133948.
22. Rong, Y.; Hu, Y.; Mei, A.; Tan, H.; Saidaminov, M.; Seok, S.I.; McGehee, M.; Sargent, E.; Han, H. Challenges for commercializing perovskite solar cells. *Science* **2018**, *361*, eaat8235.
23. Huang, L.; Ge, Z. Simple, Robust, and Going More Efficient: Recent Advance on Electron Transport Layer-Free Perovskite Solar Cells. *Adv. Energy Mater.* **2019**, *9*, 1900248.

24. Cui, P.; Wei, D.; Ji, J.; Song, D.; Li, Y.; Liu, X.; Huang, J.; Wang, T.; You, J.; Li, M. Highly efficient electron-selective layer free perovskite solar cells by constructing effective p–n heterojunction. *Sol. RRL* **2017**, *1*, 1600027.
25. Zhao, P.; Han, M.; Yin, W.; Zhao, X.; Kim, S.; Yan, Y.; Kim, M.; Song, Y.; Park, N.; Jung, H. Insulated Interlayer for Efficient and Photostable Electron-Transport-Layer-Free Perovskite Solar Cells. *ACS Appl. Mater. Interfaces* **2018**, *10*, 10132–10140.
26. Zheng, E.; Wang, X.-F.; Song, J.; Yan, L.; Tian, W.; Miyasaka, T. $PbI_2$-Based Dipping-Controlled Material Conversion for Compact Layer Free Perovskite Solar Cells. *ACS Appl. Mater. Interfaces* **2015**, *7*, 18156–18162.
27. Liao, J.-F.; Wu, W.-Q.; Jiang, Y.; Zhong, J.-X.; Wang, L.; Kuang, D.-B. Understanding of carrier dynamics, heterojunction merits and device physics: Towards designing efficient carrier transport layer-free perovskite solar cells. *Chem. Soc. Rev.* **2020**, *49*, 354–381.
28. Wu, W.-Q.; Liao, J.-F.; Zhong, J.-X.; Xu, Y.-F.; Wang, L.; Huang, J. Suppressing Interfacial Charge Recombination in Electron- Transport-Layer-Free Perovskite Solar Cells to Give an Efficiency Exceeding 21%. *Angew. Chem. Int. Ed.* **2020**, *59*, 20980–20987.
29. Li, D.; Chao, L.; Chen, C.; Ran, X.; Wang, Y.; Niu, T.; Lv, S.; Wu, H.; Xia, Y.; Ran, C.; et al. In Situ Interface Engineering for Highly Efficient Electron-Transport-Layer-Free Perovskite Solar Cells. *Nano Lett.* **2020**, *20*, 5799–5806.
30. Huang, L.; Zhang, D.; Bu, S.; Peng, R.; Wei, Q.; Ge, Z. Synergistic Interface Energy Band Alignment Optimization and Defect Passivation toward Efficient and Simple-Structured Perovskite Solar Cell. *Adv. Sci.* **2020**, *7*, 1902656.
31. Cheng, H.; Li, Y.; Zhang, M.; Zhao, K.; Wang, Z.-S. Self-Assembled Ionic Liquid for Highly Efficient Electron Transport Layer-Free Perovskite Solar Cells. *ChemSusChem* **2020**, *13*, 2779–2785.
32. Valles-Pelarda, M.; Hames, B.; García-Benito, I.; Almora, O.; Molina-Ontoria, A.; Sánchez, R.; Garcia-Belmonte, G.; Martín, N.; Mora-Sero, I. Analysis of the hysteresis behavior of perovskite solar cells with interfacial fullerene self-assembled monolayers. *J. Phys. Chem. Lett.* **2016**, *7*, 4622–4628.
33. Sadegh, F.; Akman, E.; Prochowicz, D.; Tavakoli, M.; Yadav, P.; Akin, S. Facile NaF Treatment Achieves 20% Efficient ETL-Free Perovskite Solar Cells. *ACS Appl. Mater. Interfaces* **2022**, *14*, 34.
34. Huang, C.; Lin, P.; Fu, N.; Liu, C.; Xu, B.; Sun, K.; Wang, D.; Zeng, X.; Ke, S. Facile fabrication of highly efficient ETL-free perovskite solar cells with 20% efficiency by defect passivation and interface engineering. *Chem. Commun.* **2019**, *55*, 2777–2780.

35. Bai, Y.; Chen, H.; Xiao, S.; Xue, Q.; Zhang, T.; Zhu, Z.; Li, Q.; Hu, C.; Yang, Y.; Hu, Z. Effects of a molecular monolayer modification of NiO nanocrystal layer surfaces on perovskite crystallization and interface contact toward faster hole extraction and higher photovoltaic performance. *Adv. Funct. Mater.* **2016**, *26*, 2950–2958.
36. Hu, W.; Zhou, W.; Lei, X.; Zhou, P.; Zhang, M.; Chen, T.; Zeng, H.; Zhu, J.; Dai, S.; Yang, S. Low-temperature in situ amino functionalization of $TiO_2$ nanoparticles sharpens electron management achieving over 21% efficient planar perovskite solar cells. *Adv. Mater.* **2019**, *31*, 1806095.
37. Asahi, R.; Morikawa, T.; Ohwaki, T.; Aoki, K.; Taga, Y. Visible-light photocatalysis in nitrogen-doped titanium oxides. *Science* **2001**, *293*, 269–271.
38. Chen, J.; Zhao, X.; Kim, S.; Park, N. Multifunctional chemical linker imidazoleacetic acid hydrochloride for 21% efficient and stable planar perovskite solar cells. *Adv. Mater.* **2019**, *31*, 1902902.
39. Zheng, Y.; Jiang, B.; Gao, Z.; Lin, G.; Sang, N.; Chen, L.; Li, M. Optimization of $SnO_2$-based electron-selective contacts for Si/PEDOT: PSS heterojunction solar cells. *Sol. Energy* **2019**, *193*, 502–506.
40. Peng, Q.; Guo, J.; Zhang, Q.; Xiang, J.; Liu, B.; Zhou, A.; Liu, R.; Tian, Y. Unique lead adsorption behavior of activated hydroxyl group in two-dimensional titanium carbide. *J. Am. Chem. Soc.* **2014**, *136*, 4113–4116.
41. Thirumoorthi, M.; Prakash, J.T.J. Structure, optical and electrical properties of indium tin oxide ultra thin films prepared by jet nebulizer spray pyrolysis technique. *J. Asian Ceram. Soc.* **2016**, *4*, 124–132.
42. Sajid, S.; Alzahmi, S.; Salem, I.; Obaidat, I. Perovskite-Surface-Confined Grain Growth for High-Performance Perovskite Solar Cells. *Nanomaterials* **2022**, *12*, 3352.
43. Akman, E.; Akin, S. Poly(N,N′-bis-4-butylphenyl-N,N′-bisphenyl)benzidine-Based Interfacial Passivation Strategy Promoting Efficiency and Operational Stability of Perovskite Solar Cells in Regular Architecture. *Adv. Mater.* **2021**, *33*, 2006087.
44. Krogmeier, B.; Staub, F.; Grabowski, D.; Rau, U.; Kirchartz, T. Quantitative analysis of the transient photoluminescence of $CH_3NH_3PbI_3/PC_{61}BM$ heterojunctions by numerical simulations. *Sustain. Energy Fuels* **2018**, *2*, 1027–1034.
45. Chen, X.; Lu, H.; Yang, Y.; Beard, M. Excitonic effects in methylammonium lead halide perovskites. *J. Phys. Chem. Lett.* **2018**, *9*, 2595–2603.
46. Wang, T.; Daiber, B.; Frost, J.; Mann, S.; Garnett, E.; Walsh, A.; Ehrler, B. Indirect to direct bandgap transition in methylammonium lead halide perovskite. *Energy Environ. Sci.* **2017**,

*10*, 509–515.

47. Kirchartz, T.; Rau, U. Decreasing radiative recombination coefficients via an indirect band gap in lead halide perovskites. *J. Phys.Chem. Lett.* **2017**, *8*, 1265–1271.